4-26-2012

A Modified Command Feedforward Tracking Control System Applied to the PRRR-RR Parallel Mechanism

Jeffrey A. Parkins
University of Wyoming

John F. O'Brien
University of Wyoming, obrienj@uwyo.edu

Publication Information

Parkins, Jeffrey A. and O'Brien, John F. (2012). "A Modified Command Feedforward Tracking Control System Applied to the PRRR-RR Parallel Mechanism." *Active and Passive Smart Structures and Integrated Systems* 8341, 83410N-1-83410N-15.

A modified command feedforward tracking control system applied to the PRRR-RR parallel mechanism

Jeffrey A. Parkins[a] and John F. O'Brien[b]

[a,b]Department of Electrical Engineering,University of Wyoming, Department 3295, 1000 E University Ave, Laramie, WY, 82071, USA;

ABSTRACT

The development of a prototype two degree-of-freedom parallel mechanism for application to unmanned ground vehicle target tracking is presented. The mechanism is extremely simple, decoupling the two end-effector degrees-of-freedom (DOFs) with an easily fabricated and inexpensive connection of passive joints. A summary of the parallel mechanism's kinematic design and singularity analysis is provided. A 2-DOF tracking system using a digital camera with a large time delay is presented. A command feedforward controller is designed to extend the tracking bandwidth by approximately two octaves beyond that of the feedback controller without violating causality. Experimental data is presented that shows improvement in the tracking performance by a factor of 2.4 over the feedback system alone.

Keywords: modified command feedforward, nonminimum-phase, time delay, parallel kinematic mechanism

1. INTRODUCTION

Many approaches have been taken for unmanned ground vehicle target tracking systems. Often, serial gimbal type mechanisms are used for two degree-of-freedom applications [1, 2]. Serial mechanisms require that the base actuator have sufficient torque to move the second actuator and end-effector. Parallel mechanisms remove the requirement of moving both actuators and the end-effectors with another actuator. Instead, the load of the end-effector is shared amongst actuators in a closed kinematic chain. This leads to smaller actuators, a higher bandwidth and fast, accurate motion.

In this paper a parallel kinematic mechanism is presented for the purpose of target tracking. The source of target information is a commercial digital camera based on the IEEE 1394b interface bus. This type of camera allows for the use of interchangeable optics, commodity processing hardware, and widely available software. Further, it has low cost. In exchange for these many advantages, the control scheme must deal with a large frame delay inherent in camera's processing system. It is desired that the mechanism be able to track sophisticated command inputs with a frequency out to 20 Hz. This cannot be done with a feedback controller alone as the time delay limits the bandwidth of the controller to 2.3 Hz. This leads to the implementation of a command feedforward controller to extend the tracking bandwidth to the desired 20 Hz. However, implementation of a command feedforward on a system with large time delays is difficult due to the conditions of causality.

The traditional approach for designing a command feedforward controller consists of pole-zero cancellation. However, this approach cannot be used in the case of a nonminimum-phase system. Several approaches to designing command feedforward controllers for systems with a finite number of nonminimum-phase zeros have been studied in previous work. In [3], a method is proposed for zero phase error tracking control (ZPETC). This method insures that the phase error between the input and output signals is zero for all frequencies, but does not take into account the gain errors. In [4], an approach to improve the gain and phase errors is presented. This approach utilizes a preview filter to modify the nominal command feedforward control system. A further extension of this approach is presented by Menq in [5]. This extension provides a systematic way to compensate for both gain and phase errors in the tracking system with command feedforward. The last two approaches require a preview filter and assume the nonminimum-phase in the system is due to a finite number of nonminimum-phase zeros and not a large time delay.

The system presented in this paper has nonminimum-phase due to a large time delay in the sensor, so an alternative approach to compensating for gain and phase errors over a finite bandwidth is developed. This design

Active and Passive Smart Structures and Integrated Systems 2012,
edited by Henry A. Sodano, Proc. of SPIE Vol. 8341, 83410N · © 2012 SPIE
CCC code: 0277-786X/12/$18 · doi: 10.1117/12.917513

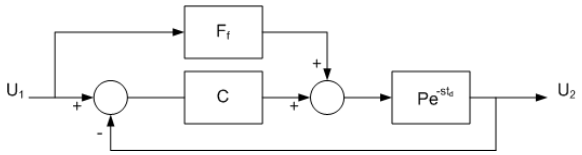

Figure 1. Command feedforward block diagram with time delay.

is driven by the development of a qualitative error expression. This paper covers an overview of the parallel kinematic mechanism, a discussion of the identification process and characterization of the camera sensor, and finally a look at the design of the control system for target tracking.

2. COMMAND FEEDFORWARD CONTROL

Traditionally, the command feedforward approach is not used for systems that are nonminimum-phase, as their inverses are either unstable or noncausal. These limitations of using command feedforward are discussed by Lurie [6]. Lurie states, "A plant with substantial pure delay would imply using feedforward with substantial phase advance which is not feasible." To overcome this limitation, while gaining performance, the nominal plant model developed from the fitting of the magnitude frequency response data was used as the starting point for the design of the command feedforward system. Investigation of the block diagram and associated closed loop transfer function led to further ideas for modifying the command feedforward control. The block diagram of the command feedforward control system is shown in Figure 1.

The close loop transfer function from input U_1 to output U_2 is:

$$\frac{U_2}{U_1} = \frac{F_f P e^{-st_d} + C P e^{-st_d}}{1 + C P e^{-st_d}} \tag{1}$$

The goal of command feedforward is to push the tracking performance beyond the bandwidth of the feedback controller alone. The goal for tracking systems is to maintain unity gain, from input to output, across the desired frequency range. With command feedforward control architectures, there are two cases where this unity gain is seen. First is in the case of large feedback and second is when the plant transfer function does not deviate much from the nominal plant model in the feedforward path [6].

3. $\underline{P}RRR - \underline{R}R$ MECHANISM

The mechanism of a $\underline{P}RRR - \underline{R}R$ parallel robot is shown in Figures 2 and 3. The naming convention is based upon the joints in a kinematic chain in the mechanism. The letters correspond to the type of joint, with "P" representing a prismatic joint and "R" representing a revolute joint. The underlined letters indicate the active actuators in the mechanism, while all others represent passive joints. This mechanism utilizes two actuators, primarily off the shelf passive joints, and a commercial off-the-shelf (COTS) camera for the purposes of tracking a given reference signal. This mechanism is extremely simple in the two independent axes of movement, leading to the two end-effector degrees-of-freedom (DOFs) being decoupled.

3.1 Architecture

The mechanism consists of two closed kinematic paths. One kinematic path consists of a prismatic actuator, a passive ball bearing revolute joint and two passive revolute pin joints ($\underline{P}RRR$). The other kinematic path is a revolute actuator in series with a single passive pin joint ($\underline{R}R$). This plant architecture has been evolved from the one used in [7, 8, 9].

3.2 Kinematics of the $\underline{P}RRR - \underline{R}R$ Mechanism

This architecture has two decoupled DOFs for the camera movement. These are designated the X-Axis in the prismatic direction of movement and the Y-Axis in the revolute direction of movement. Multivariable analysis, described later, shows the two mechanism DOFs are decoupled.

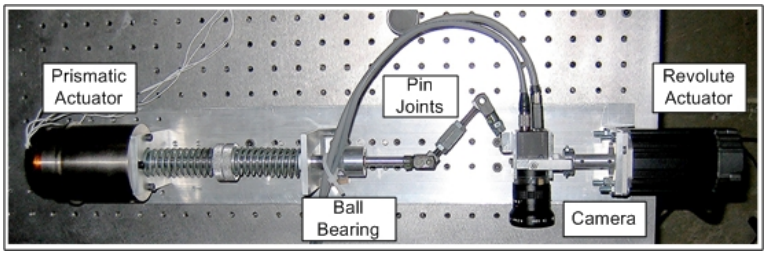

Figure 2. A photograph of the robot's actuators, joints, and sensor.

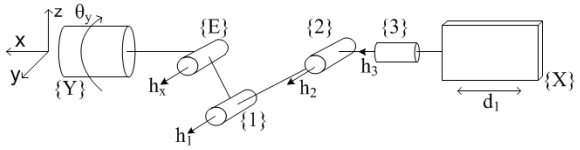

Figure 3. A schematic diagram of the robot architecture.

3.2.1 Inverse Kinematics

The kinematics of the $\underline{P}RRR - \underline{R}R$ are decoupled, leading to separate control of the X and Y axes rotations. This allows for similar kinematics analysis as shown in [8]. The Y-axis rotation is the rotation of the revolute motor that matches the desired Y-axis angle, θ_y, of the end effector. By examining the triangle made by the $\underline{P}RRR$ linkages, and the variable length, l_x, shown in Figure 4, the desired X-axis angle of rotation, θ_x, can be found. The other angles, θ_1 and θ_2 are found using the sine law.

The angle θ_0 shown in Figure 4 is the angle of the zero-configuration shown in Figure 3. This configuration also yields the zero-configuration value for the variable length, denoted l_{xo}.

$$\theta_2 = \sin^{-1}\left(\frac{l_2}{l_1}\sin\left(\theta_x + \theta_0\right)\right) \tag{2}$$

$$\theta_1 = \pi - \theta_x - \theta_0 - \theta_2 \tag{3}$$

Variable length l_x is found using the cosine law.

$$l_x = \sqrt{l_1^2 + l_2^2 - 2l_1 l_2 \cos(\theta_1)} \tag{4}$$

The X-axis displacement of the prismatic actuator required to achieve the desired θ_x is

$$d_1 = l_{x0} - l_x. \tag{5}$$

where l_{x0} is the zero-configuration value of the variable length.

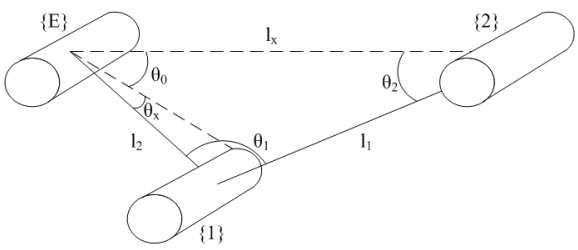

Figure 4. A schematic diagram of the $\underline{P}RRR$ triangle.

3.2.2 Velocity Kinematics

The following two matrix equations express, in general, the velocity kinematics for a parallel mechanism with a single end-effector common to all arms.

$$v_E = J_{E_a}\dot{\theta_a} + J_{E_p}\dot{\theta_p} \tag{6}$$

$$0 = J_{C_a}\dot{\theta_a} + J_{C_p}\dot{\theta_p} \tag{7}$$

The first equation represents the relationship between the end-effector velocity, v_E, and the active and passive joint velocity, $\dot{\theta_a}$ and $\dot{\theta_p}$, respectively. The second equation defines the constraints on the joint velocities for the closed-chain mechanism. There are two types of singularities in parallel robotics that relate back to these general matrix equations. These singularities are discussed in detail by Nelson et al [8].

3.2.3 $\underline{P}RRR - \underline{R}R$ Unstable Singularity

The Jacobian constraint matrix for the passive joints, J_{C_p}, must be determined for unstable singularity analysis. To begin the singularity analysis, a new reference frame is attached the robot that matches the previously defined coordinates show in 3, with the same origin, but allows for rotation around the X-axis. This fixes the kinematics for the singularity analysis as the rotation does not contribute to the unstable singularity. Additionally, the revolute joint nearest the prismatic actuator can be ignored in the analysis. This is because it is colinear with the axis of movement of the actuator and fixed to it. Therefore it also cannot contribute to the unstable singularity. As shown in Figure 3, $\vec{h_x}$ and $\dot{\theta_x}$ are the end-effector passive revolute joint axis and velocity, respectively. The two passive revolute pin joints are defined similarly with $\vec{h_1}$ and $\dot{\theta_1}$ corresponding to the axis and velocity of the first joint away from the end-effector and $\vec{h_2}$ and $\dot{\theta_2}$ corresponding to the axis and velocity of the second. Since all three axis of rotations are in the same direction, they can all be collapsed down to one vector, designated $\vec{h_1}$.

The rotational passive joint velocity constraint for this mechanism is

$$0 = \vec{h_1}\dot{\theta_x} - \vec{h_1}\dot{\theta_1} - \vec{h_1}\dot{\theta_2}. \tag{8}$$

To express the translational velocity in simplest terms the variable length vector from joint 2 to the end-effector must be defined. This vector is always constrained to the X-axis and can be expressed as

$$P_{2E} = \begin{bmatrix} p_{2E} \\ 0 \\ 0 \end{bmatrix}. \tag{9}$$

Where p_{2E} is a scalar in the $3x1$ vector. Thus, the cross product between rotation axis $\vec{h_1}$ and this vector is

$$\begin{bmatrix} 0 \\ 0 \\ -p_{2E} \end{bmatrix}. \tag{10}$$

The translational velocity constraint can be expressed as

$$0 = \hat{\vec{h_1}} P_{1E}\dot{\theta_1} + \begin{bmatrix} 0 \\ 0 \\ -p_{2E} \end{bmatrix}\dot{\theta_2}. \tag{11}$$

These constraints can be expressed as the following matrix equation.

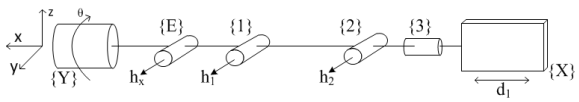

Figure 5. A schematic diagram of the $\underline{P}RRR - \underline{R}R$ Singular Configuration.

$$0 = \begin{bmatrix} 0 & 0 & 0 \\ 1 & 1 & 1 \\ 0 & 0 & 0 \\ 0 & & 0 \\ 0 & \hat{\vec{h_1}} P_{1E} & 0 \\ 0 & & -p_{2E} \end{bmatrix} \begin{bmatrix} \dot{\theta_x} \\ \dot{\theta_1} \\ \dot{\theta_2} \end{bmatrix} \tag{12}$$

The above equation is the constraint equation in the case of both actuators being locked. Simplifying the previous velocity constraint equation to

$$0 = J_{C_p} \dot{\theta_p}. \tag{13}$$

To further simplify the Jacobian, it can be noted that h_1 consists of only the Y-axis component of unit value. Thus, the resultant of cross product $\hat{\vec{h_1}} P_{1E}$ can be expressed as

$$\hat{\vec{h_1}} P_{1E} = \begin{bmatrix} 0 & 0 & h_{1_y} \\ 0 & 0 & 0 \\ -h_{1_y} & 0 & 0 \end{bmatrix} \begin{bmatrix} p_{1E_x} \\ p_{1E_y} \\ p_{1E_z} \end{bmatrix} = \begin{bmatrix} p_{1E_z} \\ 0 \\ -p_{1E_x} \end{bmatrix}. \tag{14}$$

This leaves three rows of zeros that can be removed from the previous Jacobian expression, now simplifying it to the following $3x3$ matrix,

$$J_{C_p} = \begin{bmatrix} 1 & 1 & 1 \\ 0 & p_{1E_z} & 0 \\ 0 & -p_{1E_z} & -p_{2E} \end{bmatrix}. \tag{15}$$

Mechanism configurations that cause the Jacobian to be singular are unstable. An example of this configuration is shown in Figure 5. Examining the Jacobian, it can be seen that the matrix is singular in only two configurations. First, when $p_{1E_z} = 0$, or when the mechanism is stretched out so that the two revolute pin joints lie in a plane with the end-effector revolute joint. This configuration cannot be achieved because of the limits on the stroke of the prismatic actuator. The second configuration is when $p_{2E} = 0$ or when pin joint 2 lies in the same location as the end-effector revolute joint. This configuration is physically impossible. Thus, there are no singularities in the workspace of the mechanism.

3.3 Actuation

The robot uses the same actuators as previously reported in [7]. The prismatic actuator is a BEI Kimco linear voice coil (LA28-43-000A) which can deliver approximately 300 N of force and a 3 cm displacement. The voice coil is fed by a power amplifier (AE techron LV608) with 30 $\frac{V}{V}$ of gain. A NEMA 23 electric motor, manufactured by Techic and controlled by an SST-Eclipse motor controller in torque control mode, is used as the revolute actuator.

3.4 Sensing

The primary sensor used in this experiment is a COTS camera. Target tracking software that utilizes the camera output is hosted on a standard x86 based PC, and target tracking results are conveyed to the stabilization robot's control system via analog voltages produced by a data acquisition card. Very simple image processing software capable of tracking a bright dot produced by a laser or oscilloscope has been implemented to test the camera's viability as a real-time sensor.

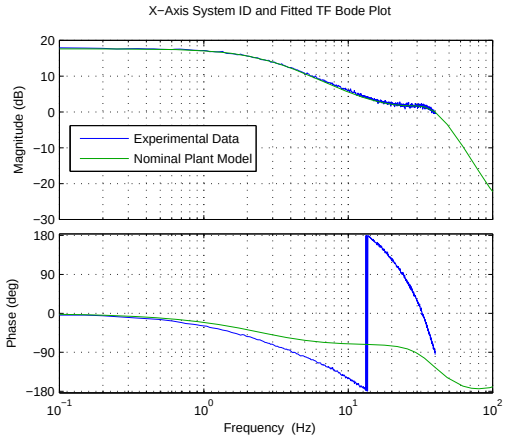

Figure 6. Nominal X-Axis plant model.

3.4.1 Camera

The FL3-FW-03S1C (Flea3) is a compact (29x29x30 mm and 58 g) IEEE 1394b interface camera manufactured by Point Grey Research. The Flea3 incorporates a Sony ICX618 1/4" CCD image sensor that can capture color video at up to 60 frames per second (fps) and monochrome video at up to 120 fps. A Pentax C60402KP C-mount lens is mated to the Flea3's interchangeable lens mount. This lens is designed for an effective focal length (EFL) of 4.2 mm when used with a 1/2" CCD. When the crop factor of the smaller 1/4" CCD is taken into account, an EFL of approximately 7.5 mm results yielding a 27° horizontal field of view. The camera is attached to the robot using a custom machined holder.

3.5 System Identification

For each DOF, a stimulus signal is injected into the actuator and a target position signal is measured. These signals are digitized and recorded by an Agilent VXI system. DataPhysics SignalCalc 6.2 is used to capture and process the resulting data. Stimuli of various amplitudes are applied and corresponding coherence and plant frequency response plots are created.

3.5.1 X-Axis Identification

A linear FM chirp with a frequency range from 0.01 Hz to 30 Hz is used to stimulate the prismatic actuator to allow system identification. A nominal plant model was derived from the experimental data by pole and zero placement to shape the frequency response diagram. An 8th order nominal model $P(s)$ is plotted in Figure 6 along with the experimental data. The zero-pole-gain (ZPK) model of $P(s)$ is: $K = 0.005941$, $Z = (-5.57, -19.1, -14.1 \pm 23.1i)$, $P = (-3.02, -3.98, -18.14 \pm 24.2i, -17.2 \pm 34.1i, -37.0 \pm 32.63i)$.

As expected, the plant transfer function is low pass. The magnitude of the response is relatively flat at 17.5 dB from 0 Hz to about 1 Hz, where it begins to roll off at approximately -10 dB/octave. From approximately 17 Hz to 33 Hz, the plant modulus remains relatively flat at around 1.75 dB. After 33 Hz, the plant rolls off as 4th order. While the modulus of the nominal plant model closely follows the measured frequency response, the phase does not. This phase discrepancy has been determined to be due to a time delay in the sensor.

Random noise generated by the Agilent VXI was displayed on the oscilloscope target, and SignalCalc was used to capture both this stimulus as well as the sensor's response. The resulting data was used to generate the corresponding frequency response graph to characterize the sensor as shown in Figure 7.

The magnitude response of the sensor is relatively constant, while the phase decreases linearly with frequency which indicates a time delay in the camera system. There is a measured phase shift of 180° at 27 Hz, and therefore a phase shift of 360° at 54 Hz. This corresponds to a time delay of 18.5 ms, or approximately two inter-frame periods at 110 fps. This large time delay in the sensor is the primary limiting factor of the controller bandwidth and provides the motivation for exploring the application of the command feedforward method to this control problem.

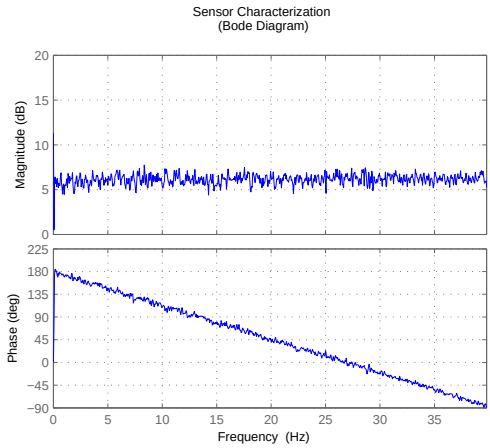

Figure 7. Sensor frequency response showing linear phase change with frequency.

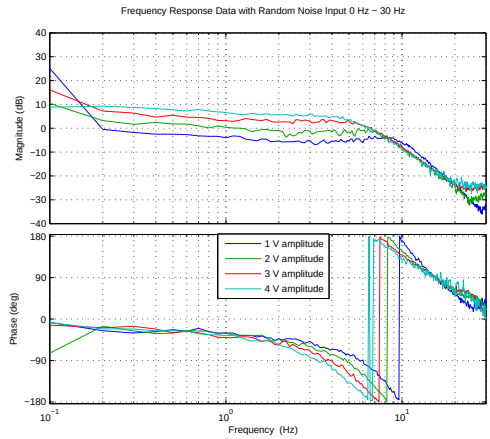

Figure 8. Frequency response of y-axis to varying amplitude white noise over frequency range of interest.

3.5.2 Y-Axis Identification

Random white noise over the frequency range, from 0.01 Hz to 30 Hz, of interest is used to stimulate the revolute actuator. This stimulus was injected at four different amplitudes, from 1 volt RMS to 4 volts RMS, to fully identify the response of the Y-Axis. This revolute axis in inherently nonlinear as shown in Figure 8. It can be seen that not only does the modulus of the response varies with varying input amplitudes, but there are two poles that shift out in frequency with lower amplitude input stimuli.

4. CONTROLLER DESIGN

The control design procedure for the tracking system begins with the design of a SISO linear feedback controller. Next a command feedforward controller is designed based only on the nominal minimum-phase plant model. Lastly, an additional block is designed in cascade with the command feedforward block to locally compensate for nonminimum-phase to obtain the final, modified command feedforward control system while maintaining the condition of causality. The modified command feedforward system is designed to track an image feature at frequencies below 20 Hz, while remaining stable with adequate gain and phase margins.

4.1 Linear Feedback Control Design

The linear feedback controller for both axes is limited to a bandwidth of 2.3 Hz due to the nonminimum-phase contribution of the camera. The design of the linear feedback controller was accomplished by shaping the return

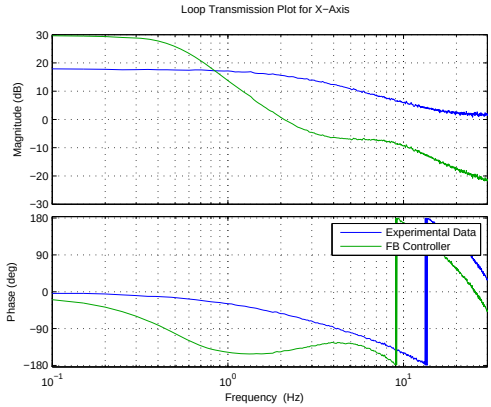

Figure 9. $\underline{P}RRR$ plant response plot and loop transmission with feedback controller in cascade

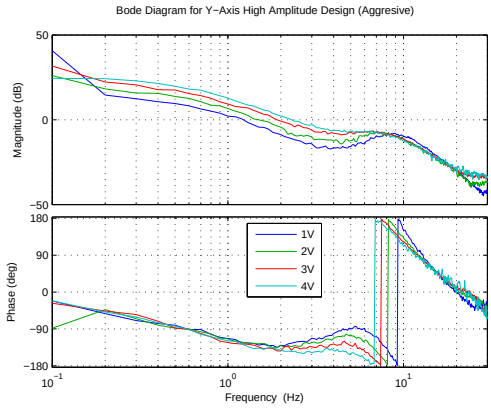

Figure 10. $\underline{R}R$ loop transmission with feedback controller designed for the high amplitude input stimulus.

ratio, T, where $T = C(s)P(s)$ and $C(s)$ is the controller and $P(s)$ is the experimental data obtained in the system identification. The results of shaping of the return ratio for the X-Axis can be seen in Figure 9.

The compensator was designed by placing poles and zeros in a transfer function model of the controller. This frequency response shaping results in a 6th order linear controller. The ZPK model of the controller is: $K = 13.0$, $Z = (-1.00, -3.50, -2.24 \pm 2.29i)$, $P = (-0.30 \pm 0.40i, -0.50, -8.50, -5.10 \pm 6.80i)$.

As the Y-Axis is inherently nonlinear, a feedback controller is designed, using the same classical approach, around the high amplitude input stimulus response and then stability is verified by plotting the response of the varying amplitudes on a Nyquist plot. Frequency shaping of the large amplitude input results in a 5th order controller. The ZPK model of this feedback controller is: $K = 67.7$, $Z = (-1.80 \pm 2.40i, -1.90 \pm 4.35i)$, $P = (-0.500, -1.25, -8.28, -4.97 \pm 6.62i)$.

The result of the feedback control design is shown in Figure 10. This figure shows the loop transmission for each varying amplitude. To verify stability at each case, the various responses were plotted on a Nyquist plot, shown in Figure 11. It can be seen that the phase margin of 30° is maintained and the gain margin increases with decreasing magnitude.

After designing the linear feedback control, the assumption that the plant is sufficiently decoupled is verified by showing the diagonal dominance of the plant, justifying the design of each linear feedback controller as an independent SISO controller. A MIMO Nyquist array plot of the system is shown in Figure 12. The small magnitude of the off diagonal plots verifies diagonal dominance of the plant, justifying the design of each feedback as independent SISO controllers for the two axes. Further, Figure 13 shows the Gershgorin discs plotted along

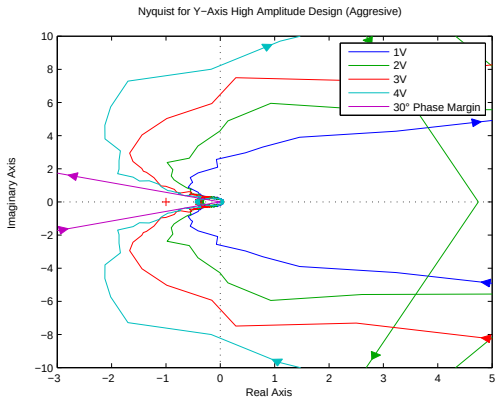

Figure 11. $\underline{R}R$ loop transmission with feedback controller designed for the high amplitude input stimulus.

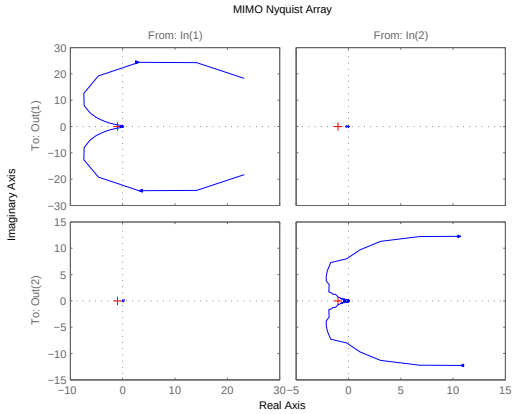

Figure 12. MIMO Nyquist Array showing diagonal dominance.

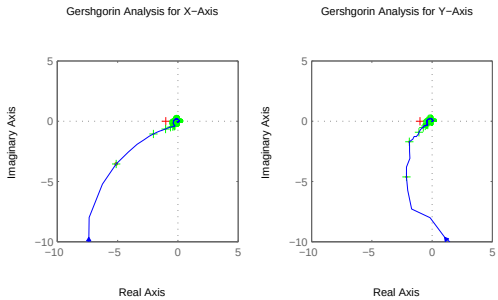

Figure 13. Plot of diagonal Nyquist Response Plots with Gershgorin discs.

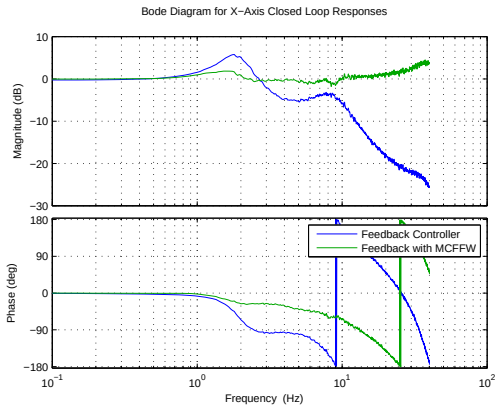

Figure 14. Close loop response of the X-Axis showing both feedback and command feedforward control.

with the diagonal Nyquist plots. As can be seen, the discs magnitude are all negligible and stay well away from the critical point. This verifies the stability of the $2x2$ multivariable system.

4.2 Command Feedforward Control Design

To increase the effectiveness of the feedforward block, while having a pure time delay in the plant, the closed loop transfer function must be broken into two parts. First, the terms from the standard feedback loop,

$$M_{FB}(j\omega) = \frac{CPe^{-st_d}}{1 + CPe^{-st_d}} \tag{16}$$

and second, the term related to the command feedforward,

$$M_{FF}(j\omega) = \frac{F_f Pe^{-st_d}}{1 + CPe^{-st_d}} \tag{17}$$

For the case of a minimum phase, proper plant, P(s), the feedforward term, F_f, would be an inversion of the plant. However, in the case of a strictly proper plant and the presence of a time delay, the feedforward term is no longer a simple inversion. Additional poles are placed in the feedforward block , F_f, to make it proper. Previously, the plant model for the $\underline{P}RRR - \underline{R}R$ system was shown to have a relative degree of four. Therefore, four zeros were added well beyond the bandwidth of the feedback controller. These zeros were all placed at nearly two decades beyond the bandwidth. The effects of the time delay are more difficult to overcome.

As the control goal is tracking over frequencies under 20 Hz, it is desired that the closed loop transfer function remain near unity gain. This suggests the following performance measure:

$$\frac{U_2}{U_1} - 1 = M(j\omega) - 1 = M_{FF}(j\omega) + M_{FB}(j\omega) - 1 = N(j\omega) \tag{18}$$

$$\alpha = \int_{\omega_1}^{\omega_2} |N(j\omega)| d\omega \tag{19}$$

It is important to note that the above error measurement cannot be used when the phase error is greater than 180°. At this point the error would appear to be growing smaller as is moves back to approach the unit value. This makes it difficult to fully capture the reduction of error from the modified command feedforward approach when the system with feedback control alone exceeds this phase error.

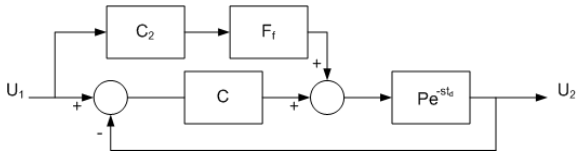

Figure 15. Modified command feedforward block diamgram with time delay

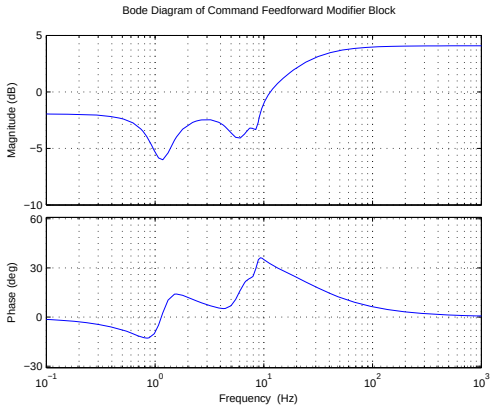

Figure 16. Bode diagram for command feedforward modifying block, C_2.

Minimizing α causes the closed loop response to approach the highest tracking performance possible. Many variables go into the development of the closed loop transfer function, causing this process of minimizing α to be done manually by adding an additional block in cascade to the nominal inverse plant model in the feedforward path. The additional block in the feedforward path is used to improve tracking response from 2 Hz to 20 Hz, extending the tracking bandwidth beyond that of the linear feedback controller alone to achieve the tracking goal. Through several iterations, the closed loop response was shaped to maintain close to unity gain from 0 Hz to 20 Hz while not violating causality. The results are shown in Figure 14.

4.2.1 Local Compensation of Nonminimum-Phase

A systematic approach is taken to develop the modification of the command feedforward path to locally compensate for some of the nonminimum-phase. This approach looks at a finite band of frequencies of interest, in this case 2 Hz to 20 Hz, and adds an additional compensator block, call it C_2, to the feedfoward path. The block diagram for this new modified command feedforward control is shown in Figure 15. The first step in this design is the placement of a first order lead. Two major considerations go into the placement of the lead. First, the lead should be placed sufficiently far from the cross over frequency of the feedback system. Second, it is important

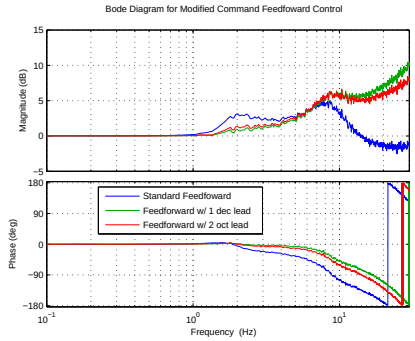

Figure 17. Bode Diagram for modified command feedforward comparison of addition of lead compensator.

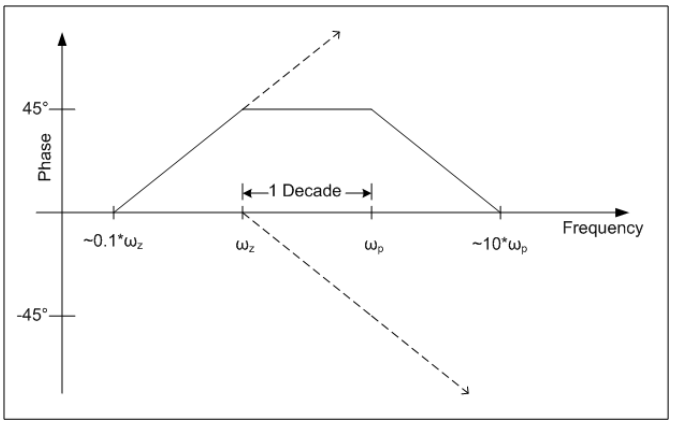

Figure 18. Example of lead of 45°

to consider the amount of phase advance that can be achieved based on the bandwidth limitations imposed by time delay.

To start, consider a frequency separation of one decade between the zero and the pole, which would provide about 45° of phase advance. An example of this lead is shown in Figure 18, where ω_z is the frequency of the zero, and ω_p is the frequency of the pole. For tracking, it is desired to achieve a phase lag of zero, suggesting that the lead be centered at the frequency we expect to see 45° of nonminimum-phase due to the sensor. However, this cannot be done as the zero in this case lies below the end of the Bode Step designed in the feedback control. The end of the Bode Step is placed at the frequency where there exists 1 radian of nonminimum-phase, or approximately 57°. Placing the zero of the lead below this point, and near the 0 dB crossover of the feedback system can lead to large gain errors as these are the frequencies where there is positive feedback. This means moving the lead to greater frequencies to allow for adequate frequency separation from the 0 dB cross over. As a starting point, moving the zero to the end of the Bode Step. In the case of the plant presented, this would place the zero at a frequency of 8.5 Hz or greater. Keeping as close to the end of the step as possible allows for greater phase advance, as the placement of the pole will be limited by the bandwidth restriction of the sensor.

The placement of the pole depends on the plant and the limitation presented by the time delay of the sensor. The greater the frequency separation of the zero and pole leads to greater phase advance, but will also introduce greater erros in the modulus of the closed loop system. In considering the bandwidth limitations of the sensor note that the greater the delay the more limited the apparent phase advance will be as the affect of a greater lead cannot be seen within the bandwidth. Less time delay allows the tracking bandwidth to be extended further, allowing for greater phase advance.

To illustrate the above approach to placing the lead, consider the following investigation using the plant presented in this paper. Consider two cases, first the case of a lead with 45° of phase advance or the placement of the pole being one decade beyond the zero and, secondly, the case of approximately 30° of phase advance, or a frequency separation of two octaves between the zero and pole. These two cases are shown in Figure 17 along with the unmodified command feedforward for comparison. As can be seen, there is little difference between the two in both phase and gain, but each is a significant improvement in phase over the unmodified command feedfoward system. This is small difference between the two cases is due to the bandwidth limitation. As the zero's of both leads are located at 8.5 Hz, the center of the leads vary. The greater advance from the one decade of separation lead is not seen because the bandwidth is limited to the region where the phase advance of both cases are close together. The other important aspect to note is the increased gain error as the phase error decreases.

After implementing the lead to locally compensate for phase error, a simple prefilter approach is used to shape the modulus and decrease the gain error. This modulus shaping does have some affect on the phase, but much of the additional phase advance is maintained. Still, it is important to look the effects on both gain and phase when shaping this modified command feedfoward control. This trade off is directly seen in the previously derived α error quantity. The end of the design is an iterative approach. After the above basic guidelines for placement, small changes are made to the lead and filters to achieve the smallest α quantity as possible by hand.

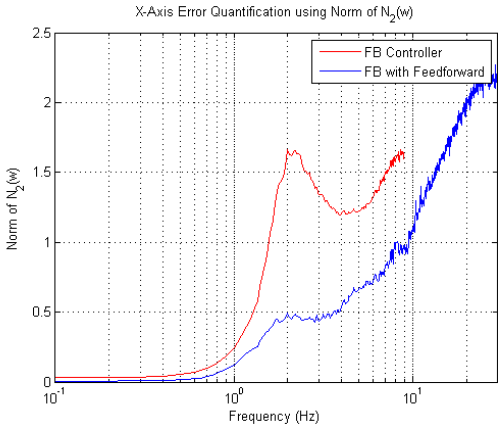

Figure 19. Plot of $|N(j\omega)|$.

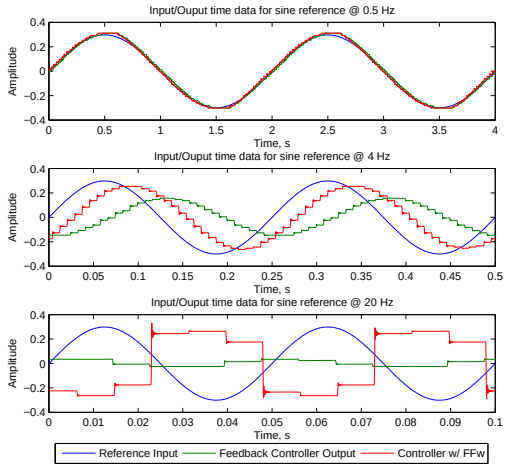

Figure 20. Tracking performance with input sine reference at various frequencies.

For the plant presented, the final design for this new block, C_2, includes a lead, with a zero at 9 Hz and a pole at 18 Hz, to locally compensate for some of the nonminimum-phase and a sixth order combination of notch filters. The ZPK model of this block is: $K = 1.60$, $Z = (-0.288 \pm 1.11, -1.68 \pm 5.76, -0.765 \pm 8.47i, -9)$, $P = (-0.46 \pm 1.05i, -2.4 \pm 5.50, -0.935 \pm 8.45, -18.0)$. A bode diagram of block C_2 can be seen in Figure 16.

Additionally, the values for $N(jw)$ are plotted in Figure 19 to show the effects of the modified command feedforward controller.

By integrating the norm of the $N(jw)$ function over the desired tracking bandwidth of 0 Hz to 20 Hz, we obtain a value for α for both the feedback and modified command feedforward systems. The feedforward has an error value of 11.25 while the modified command feedforward has an error value of 1.53. Thus the addition of the modified command feedforward controller provides 7.35 times the performance of the feedback control alone.

5. CLOSED LOOP PERFORMANCE

Several time domain tests were completed to compare the closed loop tracking performance of both the linear feedback control system and the modified command feedforward control system. Two different reference signals are used for these tests: an internally generated continuous sine reference and an externally generated discontinuous triangle reference. The first reference trajectory for testing the tracking performance is a sine reference signal generated discretely on the NI machine. The program provides the ability to vary the amplitude, frequency and phase of the reference sine. The performance was tested at three different frequencies to verify performance.

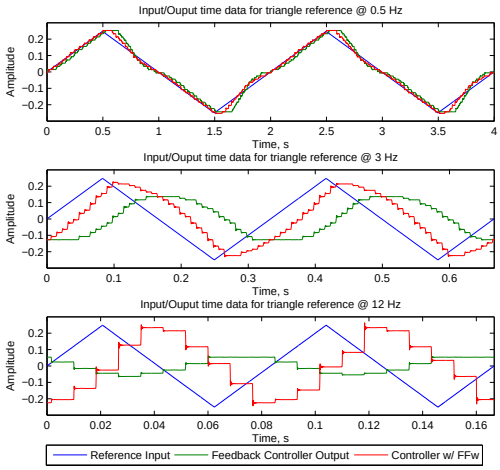

Figure 21. Tracking performance with input triangle reference at various frequencies.

First, at 0.5 Hz, well within the bandwidth of the feedback controller, then beyond the bandwidth of the linear feedback controller at both 4 Hz and 20 Hz. The results of these tests are shown in Figure 20. Similarly, the tracking performance of a discontinuous reference signal was tested. This reference trajectory consists of an externally generated triangle wave provided by an Agilent 33120 Function Generator input into the NI machine. The function generator provides the ability to vary the amplitude and frequency of the reference signal. The discontinuous tracking performance was tested at three varying frequencies, 0.5 Hz, 3 Hz, and 12 Hz. These results can be seen in Figure 21. These closed loop results verify the improvement of the target tracking, the extension of the tracking bandwidth out to 20 Hz, and the ability to track discontinuous reference signals by implementing the modified command feedforward control.

6. CONCLUSION

The simple design of the PKM leads to a decoupled system and simplifies the control design. However, the large time delay inherent to the camera sensor creates other difficulties in designing the control system for the target tracking system. A simple pole-zero cancellation approach for a command feedforward controller is insufficient to compensate for gain and phase errors in the input to output system. This fact lead to the proposal for the modified command feedforward controller. This design was accomplished through the development of a qualitative error quantification. Using this quantification of error, the tracking performance was improved by a factor of 2.4 times and extended out to the desired 20 Hz tracking bandwidth. The performance is verified through tracking experiments using both continuous and discontinuous reference signals. Additionally, it is interesting to note that although the camera system does not provide so-called hard real-time performance, these experiments have shown that it is a viable source of real-time sensing which can be used in a closed loop control system.

REFERENCES

[1] Stolle, S. and Rysdyk, R., "Flight path following guidance for unmanned air vehicles with pan-tilt camera for target observation," *22nd Digital Avionics Systems Conference, Sensing and Control* (2003).

[2] Kennedy, P. and Kennedy, R., "Direct versus indirect line of sight stabilization," *IEEE Transactions on Control System Technology* **11**(1) (2003).

[3] Tomizuka, M., "Zero phase error tracking algorithm for digital control," *ASME Journal of Dynamic Systems, Measurement and Control* **109**, 176–179 (1987).

[4] Menq, C. and Chen, J., "Precision tracking control of discrete time nonminimum-phase systems," *American Control Conference* (1992).

[5] Menq, C. and Xia, J., "Characterization and compensation of discrete-time nonminimum-phase systems for precision tracking control," *Internation Journal of Systems Science* **24**(6), 1189–1205 (1993).

[6] Lurie, B. J. and Enright, P. J., [*Classical Feedback Control with MATLAB*], Marcel Dekker, New York, NY (2000).

[7] Carruthers, D. J., O'Brien, J. F., McInroy, J. E., and Yang, Y., "Development of a voice coil-actuated limited-degree-of-freedom parallel mechanism for vibration suppression," *Proceedings of the Institution of Mechanical Engineers, Part I: Journal of Systems and Control Engineering* **223**(1), 85–94 (2009). [DOI: 10.1243/09596518JSCE599].

[8] Nelson, P. J., Carruthers, D. J., O'Brien, J. F., and McInroy, J. E., "Design and control of a two-arm parallel mechanism using revolute and prismatic actuators," *IASTED Technology Conferences* **705** (2010).

[9] Carruthers, D. J. and O'Brien, J. F., "Two degree-of-freedom parallel mechanism for high bandwidth vibration suppression and tracking," *Proc. SPIE* **7977**(797708) (2011). [DOI: 10.117/12.880064].